Progress In Electromagnetics Research M, Vol. 66, 1–10, 2018

Analysis of Polarization Interference-Type BPF Arrays for NIR Spectroscopic Imaging Utilizing All-Dielectric Planar Chiral Metamaterials

Yasuo Ohtera*, Jiyao Yu, and Hirohito Yamada

Abstract—We investigated the potential application of planar chiral metamaterials (PCMs) to near infrared wavelength filters for multispectral measurement through electromagnetic simulation. PCM assumed here was a two-dimensional sub-wavelength surface grating on a high index film with chiral unit cells. The PCM exhibits optical activity (OA) for normally incident light at a finite wavelength range. Thus, by sandwiching the PCM with a pair of linear polarizers, a polarization interference-type BPF can be constructed. We focused on an all-dielectric PCM consisting of a silicon chiral layer and a dielectric underclad layer on a silica substrate. Wavelength filtering characteristics with different bandwidths have been verified for several underclad materials such as Si_3N_4, Al_2O_3, and Si.

1. INTRODUCTION

Near infrared spectroscopy (NIRS) can acquire both quantitative and qualitative information inside the target objects by using the wavelength between 800 nm to 2500 nm. This method has been now widely used in a number of industrial fields such as agriculture, food production, medical diagnosis, pharmaceutical production, etc. [1]. The most significant merit of NIRS is its non-destructive and no-contact measuring ability. Promoted by the recent demands for imaging functionality, research and development of a NIRS imaging system by combining a focal plane array such as InGaAs sensor and a wavelength filtering element [2] have been intensively conducted. Examples of the filtering elements are holographic gratings [3], liquid crystal [4] or acousto-optic tunable filters [4, 5], filter wheel [6], and multispectral filter array (MFA) [7]. MFA is an assembly of miniature wavelength filters, spatially arranged to fit the pixels of the focal plane array. The merit of the MFA-type imaging spectrometer is its simultaneous image acquisition capability. Pictures at multiple wavelengths can be captured at a time. Therefore, it is most advantageous for the real-time monitoring of chemical reactions or outdoor monitoring of agricultural products, where temporal motion or change of targets is unavoidable. To date, various types of MFAs have been proposed as follows.

A. Fabry-Perot type multilayer filters [8].
B. Surface plasmon polariton resonance filters [9].
C. Guided-mode resonance filters [10].
D. Photonic crystal filters [11, 12].

Although a number of constructions have been demonstrated, they still have disadvantages as well as advantages. For example, Type A has a fine spectral resolution as well as good controllability of bandwidth. However, it requires highly sophisticated production process. Type B consists of a

Received 27 November 2017, Accepted 11 March 2018, Scheduled 16 March 2018
* Corresponding author: Yasuo Ohtera (ohtera@ecei.tohoku.ac.jp).
The authors are with the Graduate School of Engineering, Tohoku University, Sendai, Japan.

metallic film with a sub-wavelength array of holes, thus its production process is simple. However, sharp wavelength selectivity and application to longer wavelengths are the challenges. Type C exhibits good wavelength selectivity, but needs reflective configuration. Type D has limited wavelength coverage and requires specialized production process.

Wavelength selective filters can also be constructed by a polarization interferometer [13]. This construction consists of a pair of linear polarizers sandwiching a birefringent plate. The wavelength-dependent retardation of the plate results in a wavelength selective transmittance of the interferometer. The birefringent plate may be either linear phase plate (waveplate) or circular phase plate (polarization rotator). It has been reported that a high index film with chiral surface grating exhibited a giant circular birefringence, i.e., optical activity (OA) [14]. This kind of structures has been called planar chiral metamaterial (PCM) [15]. Intensive research on optimum grating patterns [16], utilization of metallic films [17], and extension of frequency ranges to THz regime [18] have been conducted. However, the majority of the past research focused on how to enhance OA of individual PCM. Their application to spectroscopic devices has not yet explored. The aim of this paper is to propose a PCM-based spectral filtering component, which is directly useful for multispectral imaging systems.

Generally, OA of PCM is dependent on wavelength. In most wavelengths OA is quite small, except for a limited range where the OA may exceed 90 degrees. Therefore by utilizing such OA peak to the polarization interferometer, a BPF characteristic will be realized. Because the peak wavelength of the OA is a function of the grating period of the chiral pattern, we can arrange a MFA on a single substrate by placing a number of small regions with different grating periods. This is the center concept of the multi-patterned BPF of this paper. Such a BPF array will be applicable to multispectral imaging instruments. Fig. 1 shows a schematic view of a polarization interference type BPF array. For the application to NIRS imaging, we need a transmission bandwidth of the order of a few nanometers to several tens of nanometers at a center wavelength range between 1000 to 2000 nm. Actual design has to meet this requirement by a proper choice of layer materials and dimensions.

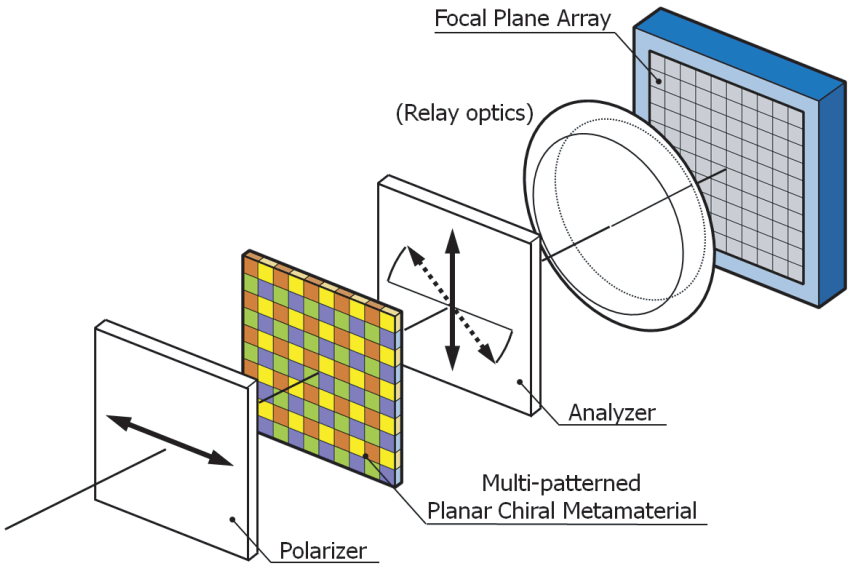

Figure 1. Schematic construction of a multispectral imaging system utilizing the polarization interference type band-pass filter array.

In the following sections we first explain the basic structure and the method of numerical simulation. Then, optical characteristics for various layer material and grating periods will be demonstrated. In Ref. [19] it was shown that the underclad layer having intermediate refractive index helped widening the OA bandwidth. Following their lines, in this paper we also investigated the effect of such underclad to search practically useful BPF constructions.

2. OUTLINE OF THE TARGET PCM STRUCTURE

A schematic view of the PCM is shown in Fig. 2. Silicon (Si) chiral layer (thickness: d_{chiral}, refractive index: $n = 3.5$) and an underclad layer (thickness: d_{clad}, refractive index: n_{clad}) are formed on a silica substrate (refractive index: $n = 1.444$). An array of gammadion pattern is assumed to be formed on the Si layer. The pattern is arranged with a square lattice geometry in x and y directions with a pitch of Λ. Width and the spacing of the gammadion arms, indicated by w_a and w_s, were both set as $\Lambda/6$, respectively. We mainly dealt with the convex pattern (emboss gammadion shape), as the concave one was found to exhibit only narrow OA peaks according to our previous study [20]. All constituent materials were assumed to be lossless and non-dispersive for simplicity. Light was assumed to be normally incident (parallel to the z axis) on the substrate from air.

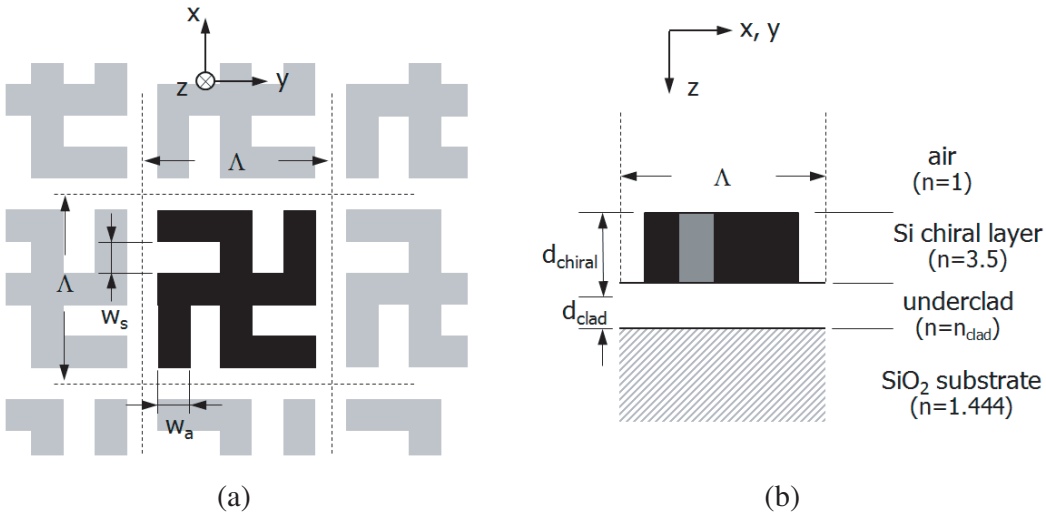

Figure 2. Schematic view of the PCM. (a) Top view, (b) cross sectional layer profile.

Konishi et al. reported that inserting an underclad beneath the chiral layer was effective for the expression of OA [19]. In this study we followed their concept and investigated three kinds of underclad materials. First one is Si_3N_4, which can be formed in the same process as the Si chiral layer. Second one is Al_2O_3. This material has high etching selectivity to Si (although separate process is needed). The final one is partially-etched type Si. Etched and remaining parts of the Si layer are expected to function as chiral and underclad layers, respectively. In this section we first describe Si_3N_4. Here we assume slightly low refractive index (n_{clad}= 1.825) made by PECVD (plasma enhance CVD).

In Ref. [15], Bai et al. indicated that two types of mechanism were responsible for the appearance of OA; one was the Fabry-Perot resonance (FP), and the other was the guided-mode resonance (GMR). Since PCM has only two layers at most, the quality factor (Q-factor) of the FP is not very high. Therefore, the OA bandwidth by FP should be relatively wide. On the other hand, GMR is known as a resonance exhibiting an extremely high Q-factor even in a single layer structure [21]. Therefore, the bandwidth of the OA peak by GMR tends to be relatively narrow.

3. METHOD OF CALCULATION

Jones matrix representation of a PCM was calculated from the transmission spectrum for the x-polarization incidence. Detailed procedure was described in Ref. [20]. In summary, we monitored the temporal waveform of the zero'th order spatial harmonic component of the transmitted light by 3-D Finite-Difference Time-Domain (FDTD) simulation [22]. The analytical space was limited to one grating period in the xy plane. The fields on the opposing xz and yz planes were connected by periodic boundary conditions. On the other hand, both ends of the z direction were terminated by Mur's 1st order absorbing boundaries [23]. Monitored waveform was Fourier transformed to get the complex Jones

vector $[a(\lambda), b(\lambda)]^T$ with λ the wavelength (T denotes transpose). The Jones vector for y-polarization incidence case could be then immediately obtained as $[-b(\lambda), a(\lambda)]^T$ without additional calculation, by considering the PCM's four-fold rotationally symmetric shape. Then, the Jones matrix, $\boldsymbol{G}$, of the PCM was obtained as follows.

$$\mathbf{G} = \begin{pmatrix} a & -b \\ b & a \end{pmatrix} \tag{1}$$

In the long wavelength region where the 1st order diffracted wave becomes cutoff ($\lambda > \Lambda/n_{clad}$), it has been known that the eigenstate of polarization (polarization which maintains its shape upon transmission) of $\mathbf{G}$ became left- and right-handed circular polarizations [15]. The power and the argument of the eigenvalues correspond to the transmission coefficient and the phase retardation, respectively. Here, the rotation angle for linearly polarized incident light is given by half of the difference of retardation for both circular polarizations. In addition, the net transmittance of the PCM sandwiched by crossed polarizers is given by $|G_{12}|^2 = |G_{21}|^2 = |b|^2$. In the following sections the OA spectrum and BPF characteristics will be shown for several underclad materials.

4. RESULTS OF SIMULATION

4.1. Silicon Nitride Underclad (Refractive Index = 1.825)

4.1.1. Overview

We examined the transmission spectrum of the BPF for different chiral layer thicknesses. Figs. 3(a), 3(b) and 3(c) show the cases where the chiral layer is thin (d_{chiral}= 440 nm), intermediate (d_{chiral}= 520 nm), and thick (d_{chiral}= 600 nm), respectively. Grating period was fixed as Λ = 960 nm. The series 'A' and 'B' in Fig. 3(a) are attributed to FP and GMR peaks, respectively. The full width at half maximum (FWHM) of the former was more than four times of the latter. The former peak shifted to the longer wavelength as the underclad thickness increased. This corresponds to the general property that the FP resonance wavelength is mainly determined by the total thickness of the chiral and the underclad layer. On the other hand, the series B represented only a small wavelength shift. This reflects the GMR's

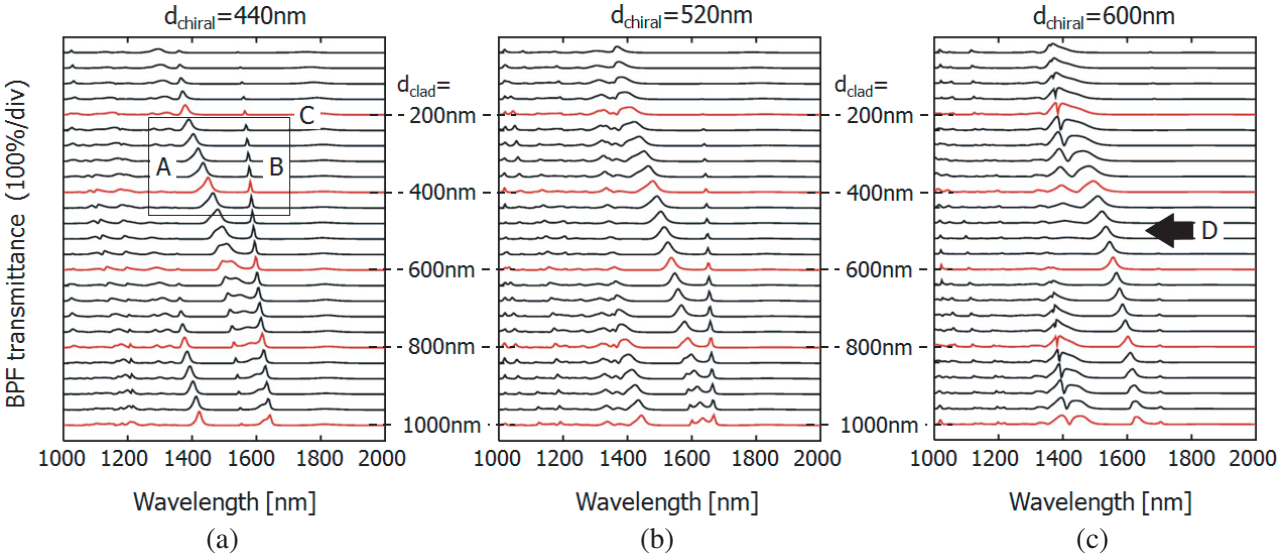

Figure 3. Calculated transmission spectra of the BPF using Si/Si_3N_4 PCM. (a) Thin Si chiral layer (d_{chiral}= 440 nm) case. Each plot correspond to different underclad thickness. Series A and B denote Fabry-Perot (FP) and guided-mode resonace (GMR) peaks, respectively. High transmittance peaks were obtained around the region C. (b) Intermediate (d_{chiral}= 520 nm), and (c) thick (d_{chiral}= 600 nm) Si chiral layers. Series D is the FP peak. Grating period was fixed as Λ = 960 nm.

nature that the resonance originates from the laterally propagating waves in the grating layer [24]. If the chiral layer was thin as Fig. 3(a), FP peak of high transmittance appeared in the region shown in 'C'. However, a narrow GMR peak coexist on the longer wavelength side. These peaks moved to longer wavelength side together as d_{chiral}increased as Fig. 3(b). In addition to this motion the GMR peak began to diminish due to the breaking of resonance condition. Of course the unimodal shape is most favorable, and this type of double peak wavelength filter was also proven to be useful for spectral analysis [25].

As the thickness of the chiral layer further increased, the GMR peaks eventually vanished, and a unimodal peak by FP remained as indicated by 'D' in Fig. 3(c). However, both the Si and Si_3N_4 layer became thicker than the double-peak structure of Fig. 3(a). If the film thickness of the Si layer was further increased, this FP peak moved to the longer wavelength side with decreasing its peak transmittance (figure not shown). Considering these characteristics, we decided to examine the structures of Fig. 3(a) (double peak) and Fig. 3(c) (single peak) in detail. In the next subsection we varied the grating period of the chiral pattern while keeping the film thickness, and calculated the transmittance as a BPF array.

4.1.2. Design of a BPF Array with Si/Si_3N_4 PCM

Figure 4(a) shows the simulated BPF spectra of thin Si/Si_3N_4 construction (double peak feature). Thickness of Si and Si_3N_4 layers were 440 nm and 400 nm, respectively. Relatively broad peak of the FWHM of 25 ∼ 30 nm accompanied by a narrow peak of FWHM of a few nanometers appeared. Fig. 4(b) is a summary of the transmittance and the bandwidth of the FP peaks. Peak transmittance exceeded 90% while the bandwidth was as narrow as 25 ∼ 30 nm. Note that the rough feature of the plots is not by the simulation error: each spectrum showed slight fluctuation along with Λ.

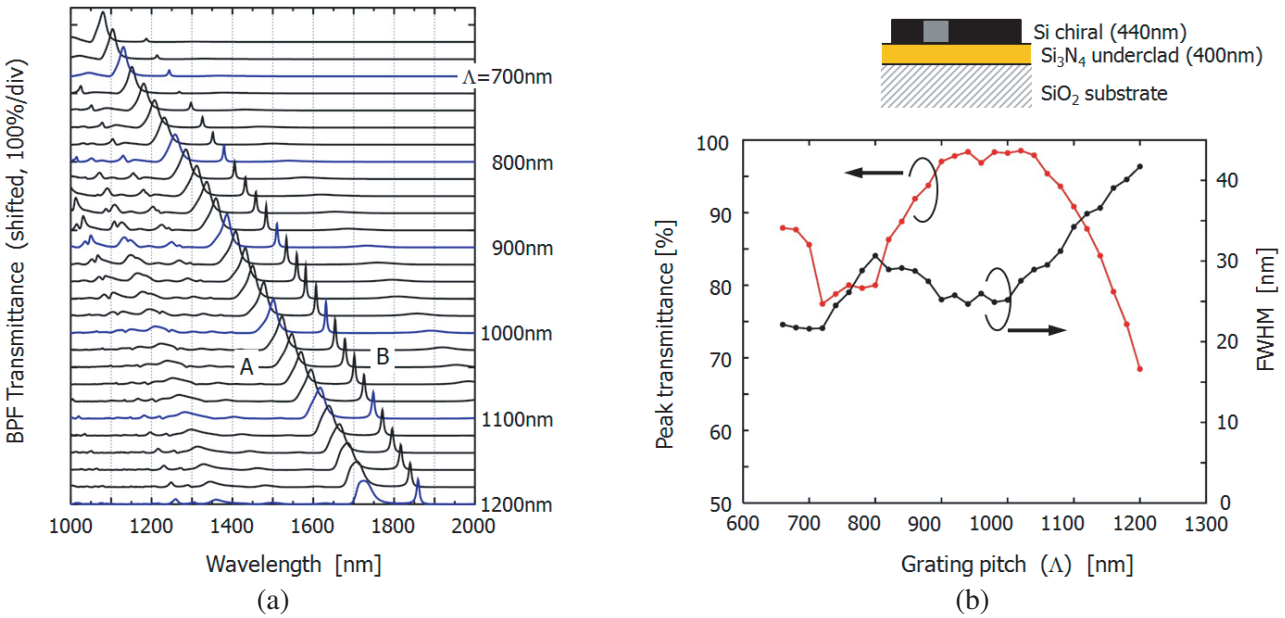

Figure 4. Designed double-peak filtering characteristics of Si/Si_3N_4 PCM. (a) Spectra for various grating period (Λ). Thickness of Si chiral and Si_3N_4 underclad layers were 440 nm and 400 nm, respectively. (b) Transmittance and bandwidth of the main peak (indicated as 'A' in the left figure).

Another set of example spectra for thick Si/Si_3N_4 construction (single peak feature) are shown in Fig. 5(a). Thicknesses of Si and Si_3N_4 layers were 600 nm and 540 nm, respectively. Here the spectrum became mostly single-moded at the cost of peak transmittance. Summary of the peak transmittance and FWHM is shown in Fig. 5(b). Transmission loss was the order of 15 ∼ 25% while bandwidth was about 25 ∼ 30 nm (almost the same as the former construction) at the grating pitch of 750 ∼ −950 nm.

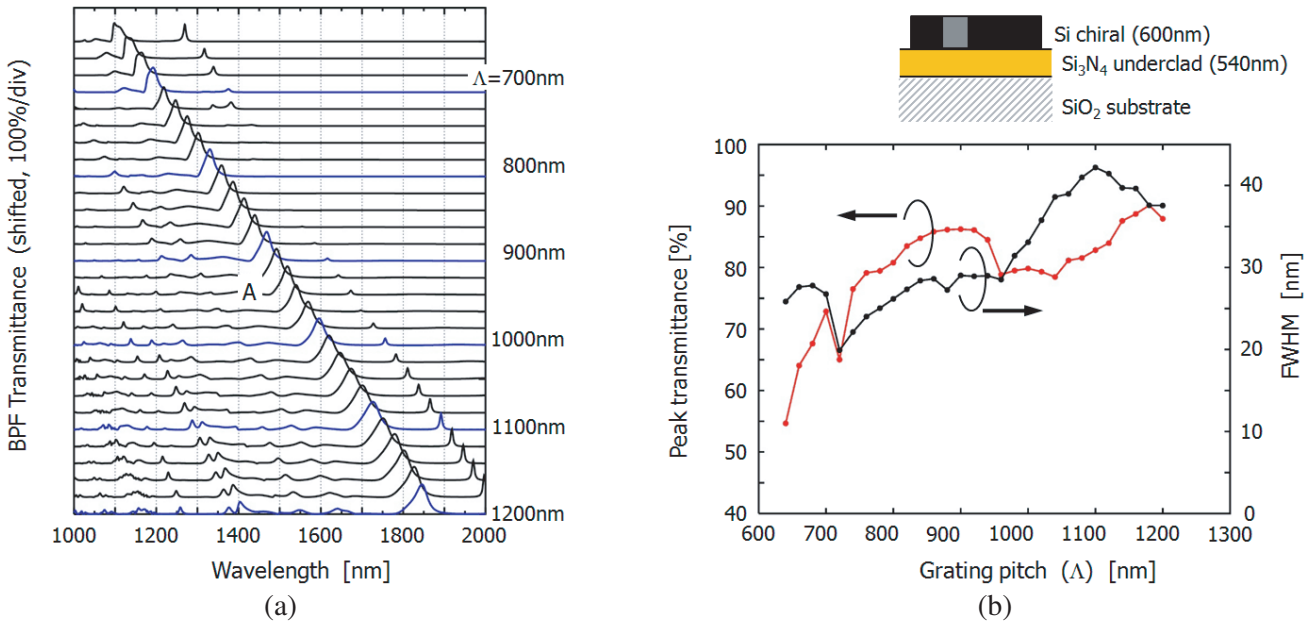

Figure 5. Designed single-peak filtering characteristics of Si/Si_3N_4 PCM. (a) Spectra for various grating period (Λ). Thickness of Si chiral and Si_3N_4 underclad layers were 600 nm and 540 nm, respectively. (b) Maximum transmittance and bandwidth of the main peak (indicated as 'A' in the left figure).

4.2. Aluminum Oxide Underclad (Refractive Index = 1.61)

Al_2O_3 film made of rf sputtering process represents refractive index of about 1.6 at visible to NIR range. The film can be hardly etched by the RIE with fluoride gases for Si, thus suitable as an etch-stop layer. Note that Bai et al. showed that the PCM with perfectly symmetric layer structure, where refractive indices of the upper and lower spaces of Si were the same, did not represent OA. We have also

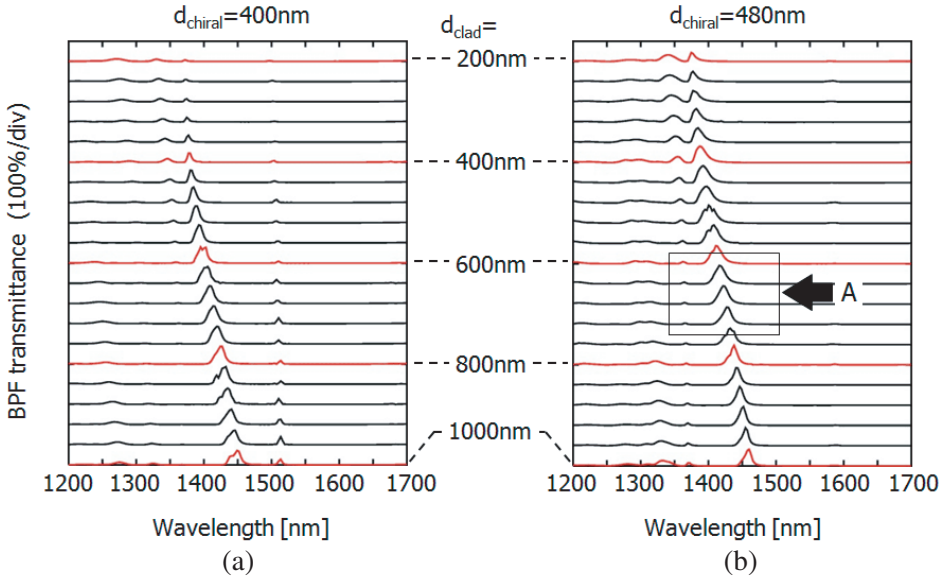

Figure 6. Calculated transmission spectra of BPFs using Si/Al_2O_3 PCM. (a) Thin Si chiral layer (d_{chiral}= 400 nm) case. Each plot correspond to different underclad thickness. (b) Thick (d_{chiral}= 480 nm) Si chiral layers. Region A indicates the unimodal construction. Grating period was fixed as Λ = 960 nm.

shown [20] that without underclad the OA peak became extremely narrow. PCM with Al_2O_3 underclad ($n = 1.610$) is close to these situations compared to the Si_3N_4 ($n = 1.825$) case. Narrower FWHM is thus expected.

Here we will show two typical constructions: relatively thin and intermediate chiral layer thicknesses. Figs. 6(a) and 6(b) show the spectra for various Al_2O_3 underclad thicknesses for d_{chiral}= 400 nm and 480 nm, respectively. Similar to the Si_3N_4 underclad, if the chiral layer was thin the GMR peak was apparent as Fig. 6(a) (small peaks near $\lambda \sim 1510$ nm). This narrow series became vague for increasing d_{chiral}as Fig. 6(b). Remaining parts of the spectra were almost flat and represent low transmittance.

Then we examined the grating period-dependence of the spectrum for d_{chiral}= 480 nm construction. Here we fixed the Al_2O_3 thickness as 720 nm (region indicated by "A" in Fig. 6(b)). Result is shown in Fig. 7(a). Their peak transmittance and bandwidth are also presented in Fig. 7(b). According to the detailed simulation we also found quite a narrow GMR peaks remained in the long wavelength side. Peak transmittance of the main peaks reached as high as 97% at $\Lambda = 1020$ nm. Bandwidths of the peaks were around $13 \sim 20$ nm for $T > 80\%$, which was almost half the Si_3N_4 case. Thus the Al_2O_3 underclad is favorable for realizing narrow banded MFAs.

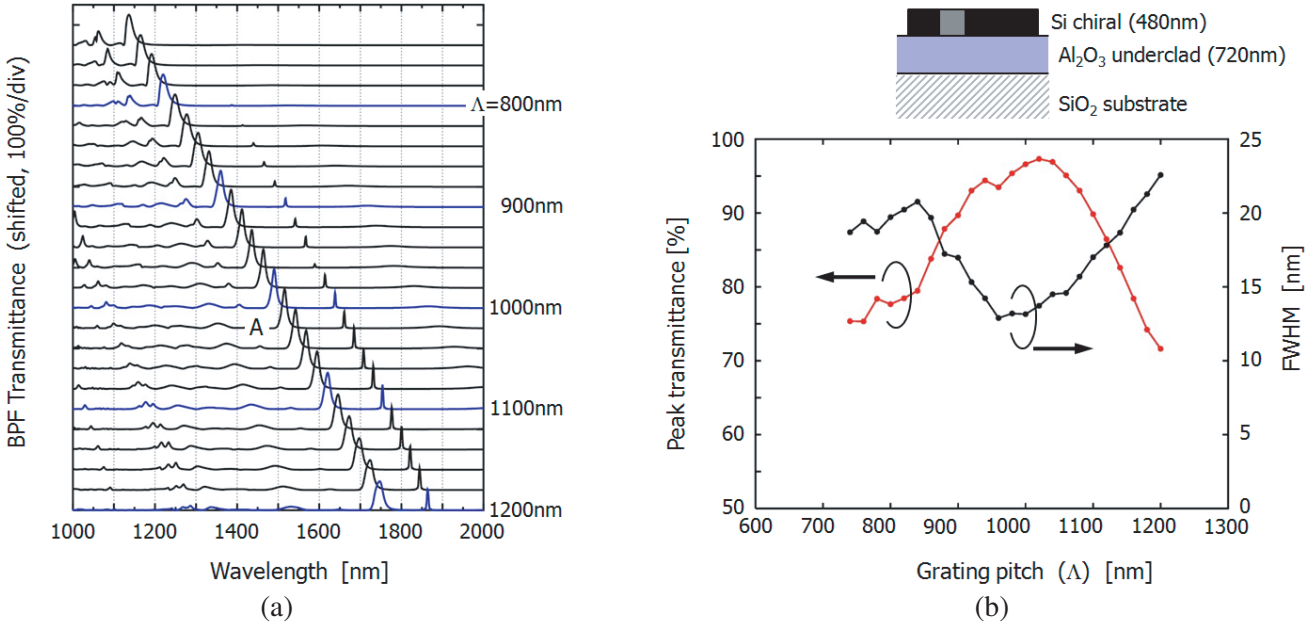

Figure 7. Designed single-peak filtering characteristics of Si/Al_2O_3 PCM. (a) Spectra for various grating period (Λ). Thickness of Si chiral and Al_2O_3 underclad layers are 600 nm and 540 nm, respectively. (b) Transmittance and bandwidth of the transmission peak 'A' in the left figure.

4.3. Silicon Underclad (Refractive Index = 3.5)

This type is assumed to be composed of a single Si layer on the silica substrate. The Si layer is to be partially etched to form a chiral pattern. The remaining, un-etched part functions as an underclad.

First, the relation between the underclad thickness and the BPF spectrum was investigated. Figs. 8(a) and 8(b) show thin (d_{chiral}= 360 nm) and thick (d_{chiral}= 480 nm) chiral thickness, respectively. One can see two key features: (1) wide bandwidth and (2) unwanted noisy transmission at the short wavelength side.

Next, transmission characteristics as a multi-patterned BPF were investigated. Etched and un-etched thicknesses of the Si layer were set as 360 nm and 160 nm, respectively. This corresponds to, relatively "clear" region indicated by "A" in Fig. 8(a). Results are summarized in Fig. 9. Although there

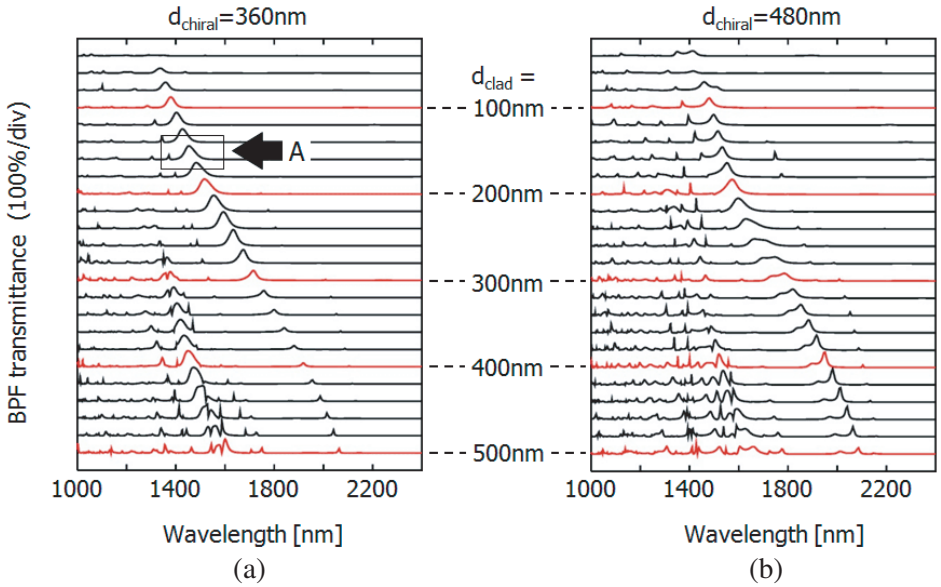

Figure 8. Calculated transmission spectra of BPFs using partiall-etched type Si PCM. (a) Thin Si chiral layer (d_{chiral}= 360 nm) case. Each plot correspond to different "unetched" Si thickness. Region A indicates high transmittance and almost unimodal construction. (b) Thick (d_{chiral}= 480 nm) chiral layer. Grating period was fixed as Λ = 960 nm.

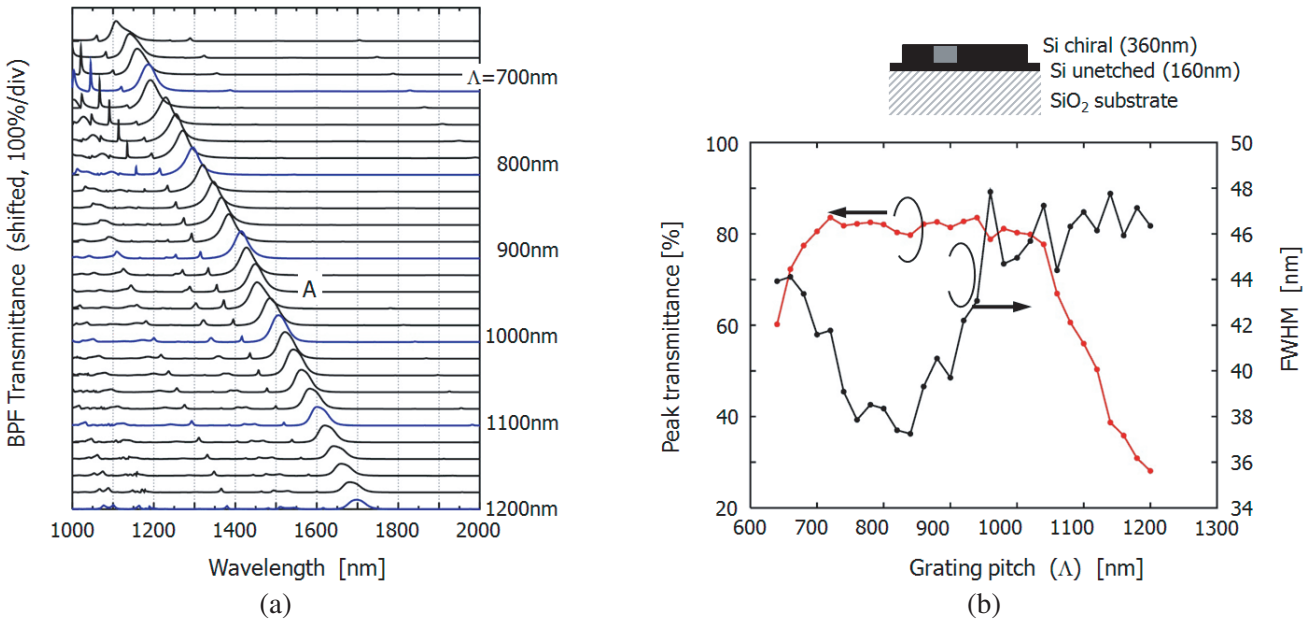

Figure 9. Designed filtering characteristics of the Si PCM. (a) Spectra for various grating period (Λ). Thickness of the etched and unetched parts of the Si layer were 360 nm and 160 nm, respectively. (b) Transmittance and bandwidth of the peak series A in the left figure.

are multiple small peaks at short wavelength side and the bandwidth of the main peaks are relatively wide, a series of BPF-like transmission bands was obtained. To see the performance of Fig. 9, peak transmittance is expected to be larger than 80% whereas the bandwidth ranges from 37 nm to 48 nm. Thus this type of film construction will be suitable for checking the rough NIR spectroscopic feature of the target: for example, concentration of alcohol in water solution, etc. [12].

Note that in all the above three example structures, we observed no significant OA peaks at long wavelength side of the main BPF peaks.

5. SUMMARY

We numerically investigated the transmission characteristics of polarization interference-type BPFs consisting of a pair of linear polarizers and all-dielectric PCMs. The PCM was assumed to be a bilayer structure on a silica substrate with underclad and top chiral layer made of Si. Feasibility of Si_3N_4, Al_2O_3 and Si as the underclad materials was studied. It was demonstrated that almost unimodal multiple filter array could be constructed by designing the PCM's grating period as $700 \sim 1200$ nm (depending on the underclad material). Optimum thickness of the Si chiral layer lies between 300 nm and 600 nm. The transmission peaks consisted of a broad one having FWHM of about $13 \sim 48$ nm, and a narrow one with the FWHM of a few nanometers. For the application to NIR spectral measurement, Si_3N_4 and Al_2O_3 were found to be promising from the viewpoint of bandwidth.

ACKNOWLEDGMENT

Y. O. would like to thank Professor Junji Yamauchi at Hosei University for his fruitful comments and continuous encouragement. This work has been in part supported by CASIO science promotion foundation.

REFERENCES

1. Osborne, B. G., T. Fearn, and P. H. Hindle, *Practical NIR Spectroscopy*, 2nd Edition, Pearson Education Ltd., England, 1993.
2. Grahn, H. F. and P. Geladi, eds., *Techniques and Applications of Hyperspectral Image Analysis*, Wiley, England, 2007.
3. Herrala, E., T. Hyvarinen, O. Voutilainen, and J. Lammasniemi, "An optoelectronic sensor system for industrial multipoint and imaging spectroscopy," *Sens. Actuators*, Vol. A61, 335–338, 1997.
4. Morris, H. R., C. C. Hoyt, and P. J. Treado, "Imaging spectrometers for fluorescence and Raman microscopy: Acousto-optic and liquid crystal tunable filters," *Appl. Spectroscopy*, Vol. 48, No. 7, 857–866, 1994.
5. Wachman, E. S., W.-H. Niu, and D. L. Farkas, "AOTF Microscope for imaging with increased speed and spectral versatility," *Biophys. J.*, Vol. 73, 1215–1222, 1997.
6. K. J. Brodbeck, A. E. Profio, and T. Frewin, "A system for real time fluorescence imaging in color for tumor diagnosis," *Med. Phys.*, Vol. 14, No. 4, 637–639, 1987.
7. Gluck, N. S., R. B. Bailey, R. de la Rosa, and R. L. Hall, "Two-color imaging by the use of patterned optical filters bonded to focal-plane-array detectors," *Appl. Opt.*, Vol. 35, No. 28, 5520–5523, 1996.
8. Lambrechts, A., P. Gonzalez, B. Geelen, P. Soussan, K. Tack, and M. Jayapala, "A CMOS-compatible, integrated approach to hyper- and multispectral imaging," *Proceedings of 2014 IEEE International Electron Devices Meeting (IEDM)*, IEDM14-261–264, 2014.
9. Chen, Q. and D. R. S. Cumming, "High transmission and low color cross-talk plasmonic color filters using triangular-lattice hole arrays in aluminum films," *Opt. Express*, Vol. 18, No. 13, 14056–14062, 2010.
10. Cunningham, B. T., "Photonic crystal surfaces as a general purpose platform for label-free and fluorescent assays," *J. Assoc. Lab. Automation*, Vol. 15, 120–135, 2010.
11. Ohtera, Y., D. Kurniatan, and H. Yamada, "Design and fabrication of multi-channel Si/SiO_2 autocloned photonic crystal edge filters," *Appl. Opt.*, Vol. 50, No. 9, C50–C54, 2011.
12. Mitsuhashi, M., Y. Ohetra, and H. Yamada, "Near-infrared imaging of liquid mixtures utilizing multi-channel photonic crystal wavelength filters," *Opt. Lett.*, Vol. 39, No. 18, 5301–5304, 2013.
13. Yariv, A. and P. Yeh, *Optical Waves in Crystals*, Sec. 5, Wiley, New York, 1984.

14. Papakostas, A., A. Potts, D. M. Bagnall, S. L. Prosvirnin, H. J. Coles, and N. I. Zheludev, "Optical manifestations of planar chirality," *Phys. Rev. Lett.*, Vol. 90, No. 10, 107404-1–107404-4, 2003.
15. Bai, B., Y. Svirko, J. Turunen, and T. Vallius, "Optical activity in planar chiral metamaterials: Theoretical study," *Phys. Rev. A*, Vol. 76, No. 2, 023811-1–023811-12, 2007.
16. M. V. Gorkunov, A. A. Ezhov, V. V. Artemov, O. Y. Rogov, and S. G. Yudin,, "Extreme optical activity and circular dichroism of chiral metal hole arrays," *Appl. Phys. Lett.*, Vol. 104, No. 22, 221102-1–221102-4, 2014.
17. Decker, M., M. Ruther, C. E. Kriegler, J. Zhou, C. M. Soukoulis, S. Linden, and M. Wegener, "Strong optical activity from twisted-cross photonic metamaterials," *Opt. Lett.*, Vol. 34, No. 16, 2501–2503, 2009.
18. G. Kenanakis, R. Zhao, A. Stavrinidis, G. Konstantinidis, N. Katsarakis, M. Kafesaki, C. M. Soukoulis, and E. N. Economou, "Flexible chiral metamaterials in the terahertz regime: A comparative study of various designs," *Opt. Mat. Express*, Vol. 2, No. 12, 1702–1712, 2012.
19. Konishi, K., B. Bai, X. Meng, P. Karvinen, J. Turunen, Y. P. Svirko, and M. K. Gonokami, "Observation of extraordinary optical activity in planar chiral photonic crystals," *Opt. Express*, Vol. 16, No. 10, 7189–7196, 2008.
20. Ohtera, Y., "Numerical analysis of artificial optical activities of planar chiral nano-gratings," *IEICE Trans. Electron.*, Vol. E97-C, No. 1, 33–39, 2014.
21. Wang, S. S. and R. Magnusson, "Theory and applications of guided-mode resonance filters," *Appl. Opt.*, Vol. 32, No. 14, 2606–2613, 1993.
22. Taflove, A. and S. C. Hagness, *Computational Electrodynamics: The Finite-Difference Time-Domain Method*, 3rd Edition, Artech House, Boston, 2005.
23. Mur, G., "Absorbing boundary conditions for the finite-difference approximation of the time-domain electromagnetic-field equations," *IEEE Trans. Electromagn. Compat.*, Vol. EMC-23, No. 4, 377–382, 1981.
24. Rosenblatt, D., A. Sharon, and A. A. Friesem, "Resonant grating waveguide structures," *IEEE J. Quantum Electron.*, Vol. 33, No. 11, 2038–2059, 1997.
25. Themelis, G., J. S. Yoo, and V. Ntziachristos, "Multispectral imaging using multiple-bandpass filters," *Opt. Lett.*, Vol. 33, No. 9, 1023–1025, 2008.